



Self-potential data inversion utilizing the Bat optimizing algorithm (BOA) with various application cases

Khalid S. Essa¹ · Zein E. Diab¹ · Salah A. Mehane¹

Received: 25 January 2022 / Accepted: 24 July 2022 / Published online: 4 November 2022
© The Author(s) 2022

Abstract

The Bat optimizing algorithm (BOA) is one of the metaheuristic algorithms and applied here to interpret self-potential (SP) data. The BOA is depending upon a bat echolocation behavior for global optimization, which the global optimum solution reached at the suggested minimum value of the objective function. The best interpretive source parameters for the subsurface structures occurred at the minimal the objective function value (global best solution). The BOA is applied to 2D SP anomaly data to estimate the characteristic source parameters (i.e., the depth to center, amplitude coefficient, origin location, geometric shape factor, and polarization and inclination angle of the causative buried structure). The BOA can be applied to single and multiple source structures in the restricted class of simple geometric shapes, which these bodies help in the validation of the subsurface ore and mineral targets. The stability and efficiency of the proposed BOA have been examined by several synthetic examples. In addition, three different real field examples from Germany and Indonesia have been successfully applied to ore and mineral investigation and geological structure studies. In general, the achieved results are in good agreement with the available borehole data and results mentioned in the literature.

Keywords Self-potential · Bat optimizing algorithm (BOA) · Mineral and ore exploration · Inclined sheets · Simple geometric shapes · Fault

Introduction

The self-potential (SP) technique represents an inactive source of the electric field that measured naturally arising potential variations in the subsurface caused by electrokinetic, thermoelectric, and electrochemical fields. Negative SP anomalies are commonly seen around mineralized zones. Additionally, SP anomalies of a minor scale are linked to other geological formations. The SP technique has been widely utilized to investigate a variety of minerals as well as subsurface geologic structure investigations. The SP technique has progressed (Revil et al. 2008; Ikard et al. 2012; Essa et al. 2020; Eppelbaum 2021). It is now widely used for sulfide, graphite, uranium, magnetite, and gold investigation

(Essa et al. 2008; Biswas et al. 2014; Kawada and Kasaya 2018; Essa 2020; Mehane 2021), archaeological investigations (Wynn and Sherwood 1984; Drahor 2004), mapping paleo-shear zones (Mehane 2015; Biswas 2017), environmental and geotechnical engineering (Hunter and Powers 2008; Xie et al. 2021), cavity discovery (Vichabian and Morgan 2002; Eppelbaum 2021), geothermal exploration (Minsley et al. 2008), coal fires detection (Shao et al. 2017; Gao et al. 2021), and monitor water movement (Soueid Ahmed et al. 2016; Kukemilks and Wagner 2021). The electrical SP technique is used in a variety of monitoring investigations, including landslides and mass sliding caused by pore pressure accumulation in the rock (Heinze et al. 2019).

Self-potential methods are favored over other geophysics-techniques in measurements, which are sensitive to fluid movements in fractured and porous rock and under natural or an applied hydraulic gradient responding to weak fluid movements (Sill 1983; Fournier 1989).

Several SP data techniques have been developed and may be classified into two categories: The SP anomaly of multi-dimensional structures (2D and 3D) falls under category I. SP inversions in multiple dimensions can be

Edited by Prof. Bogdan Mihai Niculescu (ASSOCIATE EDITOR) / Prof. Ramón Zúñiga (CO-EDITOR-IN-CHIEF).

✉ Khalid S. Essa
khalid_sa_essa@cu.edu.eg; khalid_sa_essa@yahoo.com

¹ Geophysics Department, Faculty of Science, Cairo University, P.O. 12613, Giza, Egypt

non-unique, unstable, and time-consuming to compute (i.e., Minsley et al. 2007; Rittgers et al. 2013; Oliveti and Cardarelli, 2017). Regularization techniques are standard approaches for getting a stable solution to the ill-posed inversion problems (Soueid Ahmed et al. 2016).

Category II uses geometrically basic models such as vertical cylinders, horizontal cylinders, and spheres to represent the collected self-potential anomaly. This category provides a quick quantitative interpretation intending to gauge the depth, position, and orientation parameter of the interpretative model that matches the observed data. The research introduced here belongs to this category. To delineate the depth, shape, and the polarization parameter of the causal source body from the measured SP anomaly, several quantitative techniques have been well known for category II (i.e., Yüngül, 1950; Banerjee, 1971; Rao and Babu 1983; Abdelrahman et al. 2004; Essa and Mehane, 2007; Soueid Ahmed et al. 2013; Essa 2019; Elhussein 2021). The drawback of these approaches focused on subjectivity, which may lead error in appraising the source parameters of the subsurface causative structures (Mehane 2014).

Using simple geometric models, several numerical and graphical approaches for elucidating self-potential data were developed. For example, Abdelrahman et al. (2009) presented a graphical approach to estimate the shape and depth to the center of the subsurface structures using the second-order moving average operator. Santos (2010) employed the particle swarm approach to invert SP anomalies using basic geometries. Mehane (2014) used the conjugate gradient minimizer in the dimension of the non-logarithmic and logarithmic parameters to build a regularized system for interpreting SP data. Di Maio et al. (2017) established a spectrum analysis method based on the periodogram, Multi-Taper, and Maximum Entropy methods for a full SP data interpretation using simple-geometric bodies. Sungkono (2020) introduced a global optimization technique using micro-differential evolution (MDE) to invert self-potential data comprising simple geometric shapes and inclined sheets.

Many metaheuristic-inspired algorithms have been established in recent decades to handle complicated issues, for example, the genetic algorithm (GA) (Di Maio et al. 2019), the particle swarm algorithm (PSO) (Pekşen et al. 2011), the global optimizing algorithm of simulated annealing system (Sharma and Biswas 2013), and the ant colony optimizing algorithm (Srivastava et al. 2014). These algorithms are popular among researchers because of their adaptability and ability to cope with a wide range of issues compared to standard optimization approaches. Bat optimizing algorithm (BOA) represents one of the newly proposed metaheuristic algorithms that have been applied in geophysical investigations, i.e., seismic refraction (Poormirzaee 2017; Poormirzaee et al. 2019; Essa and Diab 2022).

Several swarm intelligence algorithms have been developed and applied to various real-world problems to date, but the use of the Bat optimizing algorithm (BOA) in geophysical data analysis is relatively recent. BOA is the first algorithm of its kind in the field of optimization and computational intelligence since it uses frequency tuning. Fister (2013) concluded that BOA outperforms PSO after conducting various experiments on the implementation of the bat algorithm. Although methods like genetic algorithms (GA) and PSO can be quite beneficial, they still have certain limitations when it comes to multi-modal optimization issues (Yang and He 2013). The BOA has many advantages: one of the major advantages of the BOA is that it may give extremely rapid convergence at a relatively early stage by transitioning from exploration to exploitation. This makes it an effective method for applications requiring a rapid answer, such as classifications. BOA can use as a global optimizer as well as a local optimizer. BOA has ability to handle multi-model problem efficiently. BOA utilizes controlling parameter to update parameter as the iteration progresses. BOA is maintaining the diversity of solutions in the population. The drawbacks of BOA lie in the following: it has a lack of good exploration. It required the parameter tuning to achieve better search output. It needs an improved control strategy to switch between exploration and exploitation.

In the current work, we applied a Bat optimizing algorithm (BOA) approach for interpreting self-potential data recorded along with 2D profiles by a certain basic geometrical (i.e., vertical and horizontal cylinders, spherical shaped models, inclined sheets) as well as multi-source models. The goal of the current work is to invert the self-potential data (i.e., appraising the depth (z), location of the source origin (x_0), the amplitude coefficient (K), polarization and inclination angles (θ & φ), and the shape type (q)). The best-interpreted model parameters are obtained corresponding to the minimum normalized root-mean-squared error (NRMSE) of the objective function after reaching the global best solution. The present BOA approach is applied to different field examples around the world for mineral exploration and geological structure delineation (i.e., fault).

The paper structure is prepared as follow: Sect. **Bat optimizing algorithm (BOA)** covers the fundamentals of echolocation plus the conventional formulation of the BOA. Section **Methodology** delivers a brief explanation of how to invert SP data using the BOA. Section **Methodology** describes the forward modeling and formulation of the proposed BOA. Section **Numerical datasets test** provides that the proposed BOA approach is verified on numerical examples (including free and noisy examples, investigating the interference multiple model effects). Section **Field datasets test** discusses the applicability of the proposed BOA on different real field examples. Finally, Sect. **Conclusions**

provides conclusions that summarize the objective of the proposed BOA approach.

Bat optimizing algorithm (BOA)

The Bat optimizing algorithm (BOA) is a metaheuristic optimization offered by Yang (2010). The BOA is relied on the echolocation behavior of micro-bats. Microbats utilize echolocation to find their nest, evade obstacles, and follow prey in the dim. These bats generate an extremely loud sound pulse in the 8–10 kHz range and listen for echoes from surrounding objects. Every pulse takes a fraction about 10 ms. The pulse rate of Bats increases while their sound loudness decreases when they are approaching prey or an object (Yang 2010). Consequently, microbat echolocation activity may be represented in a way that optimizes objective functions. The main rules of the BOA can be shortened in three steps: (1) Bats utilize echolocation to assess distance; (2) Bats locate their objects by flying at a stable frequency in the range of $[F_{\min}, F_{\max}]$ with an initial velocity (V_i) at position (X_i); and (3) The loudness (L_i), and emission rate (r_i), which differ depending on the space amongst the bats and the target.

Generally, the wavelength spectrum $[K_{\min}, K_{\max}]$ refers to the frequency range $[F_{\min}, F_{\max}]$. As a result, adjusting the frequency or wavelength can be used to change the movement range of bats in an optimization issue. Consequently, choosing the right frequency or wavelength range is crucial, and it should be chosen to match the scale of the region of curiosity before harmonizing down to lower ranges. Next running the procedure with various parameters, the spectrum of $[0, 0.5]$ was calculated as the best frequency range in this investigation. The pulse rate, r_i , can be anywhere between 0 and 1, with 0 indicating no pulses and 1 indicating the maximum emission rate. The vicinity of the object or target determines the range. Additionally, the initial loudness, i.e., L_i , should normally within the domain of $[1, 2]$ (Yang 2010). The loudness of the bats decreases as they approach their victim, while the emission rate increases. The Bat algorithm can only update the loudness and emission rates if the new solutions develop, inferring that the bats are approaching the optimum solution (Fister et al. 2013).

The effects of the optimizing tuning parameters of the frequency (F_i), Loudness (L_i), and rate of pulse emission (r_i) on the rate of BOA convergence were studied (Fig. 1) using different ranges of each parameter. The influence of each set of (F_i , L_i , and r_i) parameters on the convergence rate and convergence behavior is shown in Fig. 1. Figure 1 suggests that the optimum set is that of ($F_i = [0, 5]$, $L_i = 1.0$ and $r_i = 0.9$), which has a minimum NRMSE of the objective function than other sets and gives a fast convergence to the optimum solution. Note the initial speed (V_i) at position

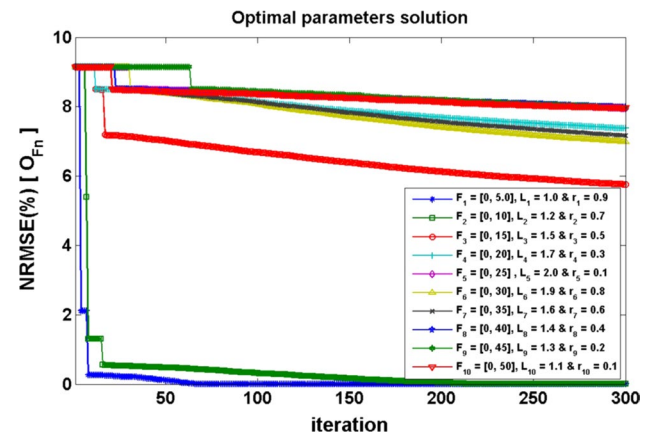


Fig. 1 Effect of different sets of optimization parameters (F_i , L_i and r_i) on the convergence rate and behavior of the BOA approach

(X_i) was set to zero at the beginning of the BOA inversion process. The performance of the BOA technique to obtain the optimal model parameters of the assumed model (i.e., synthetic data example model-1) measured using MATLAB function "tic & toc." It takes less than 50 s on ordinary computer. The result indicates that the BOA algorithm is faster than the other metaheuristic algorithms (PSO, CS, and ABC) (Khari et al. 2020).

The relationship between algorithm parameters is depicted in the equations as follows:

$$F_i^t = F_{\min} + (F_{\max} - F_{\min})\beta \quad (1)$$

$$V_i^{(t+1)} = V_i^t + (X_i^t - X_{\text{best}})F_i^t \quad (2)$$

$$X_i^{(t+1)} = X_i^t + V_i^{(t+1)} \quad (3)$$

$$L_i^{(t+1)} = \alpha L_i^t \quad (4)$$

$$r_i^t = r_i^0 [1 - \exp(-\gamma\tau)], \quad (5)$$

where F_i is the frequency of i th bat which is updated in every iteration, β is a random vector of uniform distribution between $[0, 1]$, and X_{best} is currently the global best solution among the whole bat numbers, α and γ are constants, $0 < \alpha < 1$ and $\gamma > 0$, and τ is the scaling factor.

The BOA utilizes a random path to produce novel solutions from every chosen best solution in the local search, as follows:

$$X_{\text{new}} = X_{\text{old}} + \epsilon A^t, \quad (6)$$

where $\epsilon \in [-1, 1]$ represents a randomly numbers, and L^t represents the mean loudness of the whole bat numbers at the present stage.

Methodology

It is critical to acquire correct findings for the subsurface model parameters to match the observed data when interpreting self-potential data. As a result, a large-capacity inversion method is required to get appropriate assessments of subsurface model parameters as depth, position, and shape of the buried body, among others. Metaheuristic inversion algorithms have shown to be beneficial in a variety of case studies. Most metaheuristic inversion algorithms are easy, quick, and more efficient than traditional inversion algorithms.

In this research work, we developed a MATLAB code to invert self-potential data based on the BOA (Yang 2010). Depth (z), location (x_0), polarization angle (θ), inclination angle (φ), body shape (q), and the amplitude coefficient (K) are the most critical characteristics that impact self-potential data anomaly. As a result, these parameters are searched in the suggested inversion technique to identify an acceptable subsurface model that fits the real data.

In particular, the place of every bat in search space signifies a solution. Bats flying haphazardly in search space and apply a solution in each iteration process. The location of every bat is determined using the best locations. The location with the lowest misfit of the NRMS of the objective function is picked as the best solution (X_{best}). In this study, the BOA inversion program was initially evaluated on a variety of numerical datasets. After that, it was tested on real field datasets. The search range should be adopted to simulate more realistic cases where a priori information is absent. Therefore, the search space is chosen in both synthetic and real datasets based on the objective function (O_{Fn}) where the search range for the model parameter

which will give the minimum O_{Fn} will be selected as the suitable search range.

The SP effect (mV) of simple geometric bodies such as vertical & horizontal cylinders models and spheres model at a stationary point $P(x_j, z)$ across 2D profile (Fig. 2a, b and c) is provided by (Yüngül 1950; Mehane 2014):

$$V(K, x_j, x_0, z, \theta, q) = K \frac{(x_j - x_0) \cos \theta + z \sin \theta}{\left[(x_j - x_0)^2 + z^2 \right]^q}, \quad (7)$$

$$j = 1, 2, 3, \dots, n,$$

where x_j (m) denotes the measurement station coordinates along a profile (Fig. 2), x_0 (m) is the origin/center point of source model, z (m) is the depth of buried source, K ($mV \cdot m^{2q-1}$) denotes the amplitude coefficient (moment of the electric dipole), the unit of which is dependent upon the shape factor (Abdelrahman et al. 2006). θ (degrees) denotes the angle of polarization, q (dimensionless) represents the shape factor, and n denotes the data points.

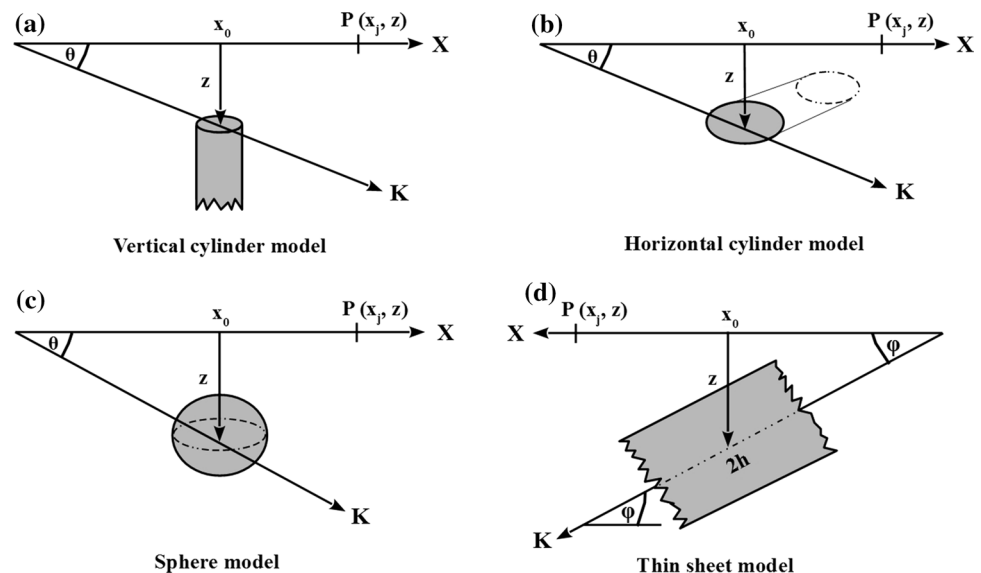
Also, the SP for a 2D inclined thin sheet (Fig. 2d) (Sundararajan et al. 1998; Essa and Elhussein 2017) is expressed as:

$$V(K, x_j, x_0, z, h, \varphi) = K \ln \left\{ \frac{[(x - x_0) - h \cos \varphi]^2 + [z - h \sin \varphi]^2}{[(x - x_0) + h \cos \varphi]^2 + [z + h \sin \varphi]^2} \right\}, \quad (8)$$

$$j = 1, 2, 3, \dots, n$$

where K (mV) represents the amplitude coefficient ($= \frac{I\rho}{2\pi}$, I denotes the current density, ρ denotes the circumference resistivity), φ (degree) denotes the angle of inclination, h (m) denotes the thin sheet's half-width.

Fig. 2 Configurations of simple geometric-shaped models: **a** vertical cylinder model, **b** horizontal cylinder model, **c** sphere model, and **d** 2D infinitely inclined thin sheet



For the full interpretation using the BOA, the misfit objective function (O_{Fn}) between observed (measured) and calculated (estimated) model response is:

$$O_{Fn} = 100 \sqrt{\frac{1}{N} \sum_{j=1}^N \left[\frac{V_o - V_c}{V_o} \right]^2}, \quad (9)$$

where N characterizes the total data points numbers, V_o represents the observed SP data and V_c represents the calculated SP response. Once a summation is approaching zero or smaller than one, the misfit increases, according to Eq. 9. Although such a circumstance is unlikely to arise with SP data, it should be avoided. In case of several data points around a zero crossing, for example, a possible gradient anomaly, the data might pose problems. To deal with such a scenario, a distinct form of misfit is well known as (Kaikonen and Sharma, 1998):

$$O_{Fn} = 100 \sqrt{\frac{1}{N} \sum_{j=1}^N \left[\frac{V_o - V_c}{\text{abs}(V_o) - \text{Max}(V_o) - \text{Min}(V_o)} \right]^2}. \quad (10)$$

Equation 10 has very good results are obtained when applying the proposed BOA technique for the inclined thin sheet model. Initially, Eqs. 9 and 10 are employed to compute misfits, and afterward the bat with a minimum misfit function is selected as the X_{best} . The BOA fundamental processes can be seen using the pseudocode in Fig. 3 and the flow chart in Fig. 4.

```

Define Objective Function  $O_{Fn}(x_i)$  [equation (9)]
Initialize the bat population  $X_i$  ( $i = 1, 2, \dots, n$ ) and  $V_i$ 
Define pulse frequency  $Q_i$  at  $X_i$ 
Initialize pulse rates  $r_i$  and the loudness  $L_i$ 
while ( $t < \text{Max number of iterations}$ )
    Generate new solutions by adjusting frequency, and updating velocities
    and locations/solutions [equations (2) to (4)]
    if ( $\text{rand} > r_i$ )
        Select a solution among the best solutions Generate a local
        solution around the selected best solution
    end if
    Generate a new solution by flying randomly
    if ( $\text{rand} < L_i$  &  $O_{Fn}(X_i) < O_{Fn}(X_{\text{best}})$ )
        Accept the new solutions
        Increase  $r_i$  and reduce  $L_i$ 
    end if
    Rank the bats and find the current  $X_{\text{best}}$ 
end while

```

Fig. 3 Bat optimizing algorithm (BOA) pseudo code (modified after Yang 2010)

Numerical datasets test

To measure the efficiency and rationality of the proposed BOA approach, it was examined on different numerical SP datasets. The numerical example responses are confined to the delimited class of the basic geometrical shapes (vertical cylinder, horizontal cylinder, and spheres) as well as to the inclined thin sheet. Firstly, the developed algorithm is tested on noise-free numerical examples, and then, the inversions are performed on noisy data for multiple sources to study the interference effect of neighbor structure and fault.

Model-1: Interference and multiple structure effects

The observed SP effect due to isolated anomalies of buried sources can be impacted by an interference influence (that is, the action of surrounding multiple structures) in specific geologic contexts (Mehanee and Essa, 2015). We computed the composite self-potential response (using formula (7)) of two surrounding geologic sources, namely a horizontal cylindrical model with [$K_1 = 700$ mV.m, $z_1 = 12$ m, $x_{o1} = -50$ m, $\theta = -35^\circ$ and $q_1 = 1$] and a sphere model with [$K_2 = 2500$ mV.m², $z_2 = 7$ m, $x_{o2} = 50$ m, $\theta = -45^\circ$ and $q_2 = 1.5$], along a profile length of 200 m (Fig. 5a) to test this influence on the stability of the distinctive parameters deduced from the BOA algorithm presented here. Applying the procedure of the BOA algorithm described before, the calculated self-potential response of the two models is shown in Fig. 5a. The obtained average loudness of the composite anomaly is revealed in Fig. 5b, while the emission rate of bat for the composite anomaly is exposed in Fig. 5c. The NRMSE of the global best solution (min objective function, O_{Fn}) is obtained in Fig. 5d, and the average NRMSE of all the bats is shown in Fig. 5e. Figure 5 and Table 1 show that the two recovered model parameters of the two introduced models are identical to the true ones. The relative error (RE) and standard deviation (SD) of the recovered parameters are illustrated in Table 1. The RE and SD can be computed using these formulas:

$$RE = \left| \frac{v_R - v_A}{v_A} \right| \times 100\%, \quad (11)$$

where the v_A is the actual true value and v_R is the recovered value.

$$SD = \sqrt{\frac{\sum_{i=1}^N (v_i - \bar{v})^2}{N - 1}}, \quad (12)$$

where the v_i is each value of the population parameter, \bar{v} is the mean value of population and N in the total number of populations or data points.

Fig. 4 Flow chart steps of the BOA

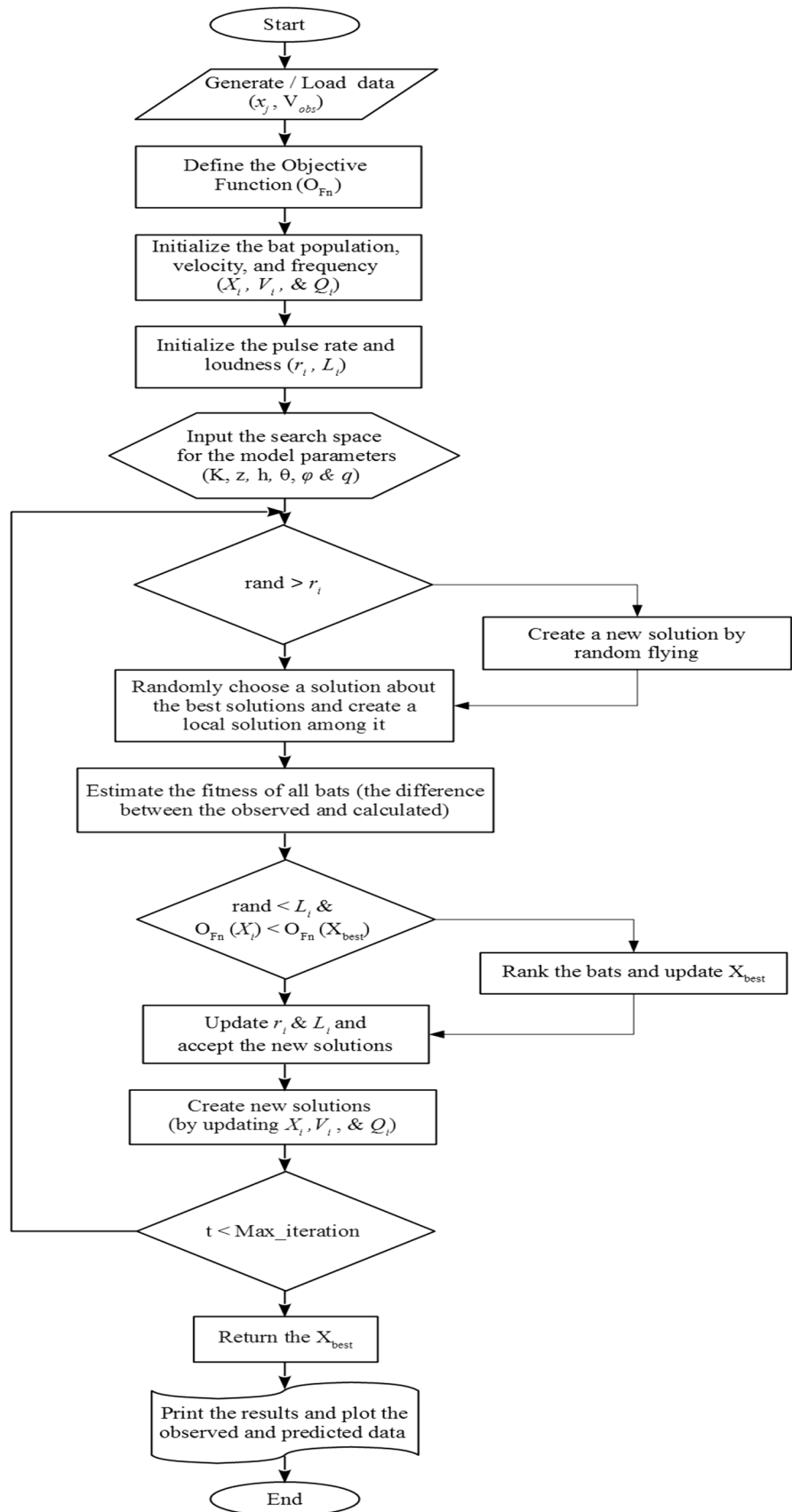


Fig. 5 Model-1: Interference and multiple structure effect. **a** The composite SP anomaly generated by horizontal cylinder and sphere model (true model parameters), as well as the calculated SP response of them (recovered model parameters) using the BOA, **b** loudness of the bats, **c** emission rate of the bats, **d** NRMSE of the global best solution (O_{Fn}) of the bats versus the iteration numbers, and **e** the average NRMSE of all the bats

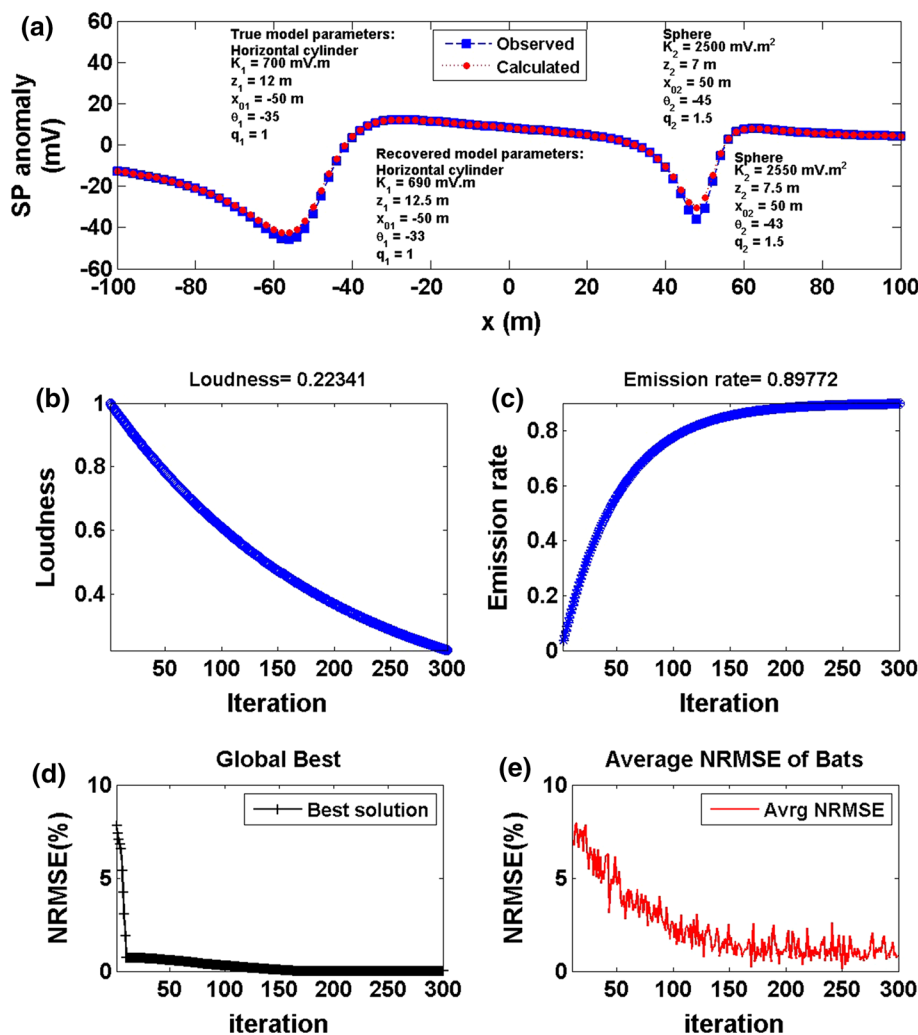


Table 1 Model-1: True and recovered model parameters of the composite interference SP anomaly of a horizontal cylinder and a sphere model with corresponding RE for each model parameters using the BOA

| Model parameters | True value | | Search range | Recovered value | | RE (%) | | O_{Fn} |
|-----------------------|---------------------------|--------------|--------------|---------------------------|------------------|---------------------------|--------------|---------------|
| | Horizontal cylinder model | Sphere model | | Horizontal cylinder model | Sphere model | Horizontal cylinder model | Sphere model | |
| K ($mV.m^{2q-1}$) | 700 | 2500 | 100:3000 | 690 ± 59.83 | 2550 ± 60.00 | 1.43 | 2.00 | $4 * 10^{-8}$ |
| z (m) | 12 | 7 | 1:15 | 12.5 ± 0.59 | 7.5 ± 0.60 | 4.17 | 7.14 | |
| x_o (m) | -50 | 50 | -100:100 | -50 ± 2.65 | 50 ± 2.65 | 0 | 0 | |
| θ ($^\circ$) | -35 | -45 | -5:-90 | -33 ± 3.35 | -43 ± 3.34 | 5.71 | 4.44 | |
| q | 1 | 1.5 | 0.5:1.5 | 1 ± 0.40 | 1.5 ± 0.25 | 0 | 0 | |

The outcomes concluded that the BOA algorithm is more stabilized and accurate in the case of multi-structures depending upon the extent of the surrounding effect.

To further investigate the procedure of BOA on multi-structure and surrounding effects, we contaminated the composite SP response (Fig. 5a) with a Gaussian noise

level of 20% (Fig. 6a). Figure 6b, c presents the average loudness and emission rate of the bat to the overall composite SP anomaly, respectively. Figure 6d, e represents the NRMSE of the global best solution (min objective function, O_{Fn}) and the average NRMSE of all the bats, respectively. Figure 6a and Table 2 illustrate that the calculated

Fig. 6 Model-1: Noisy interference and multiple structure effect. **a** The noisy composite SP anomaly produced by data set exposed in Fig. 5a after adding 20% random Gaussian noise (true model parameters), as well as the calculated SP response of them (recovered model parameters) using the BOA, **b** loudness of the bats, **c** emission rate of the bats, **d** NRMSE of the global best solution (O_{Fn}) of the bats versus the iteration numbers, and **e** the average NRMSE of all the bats

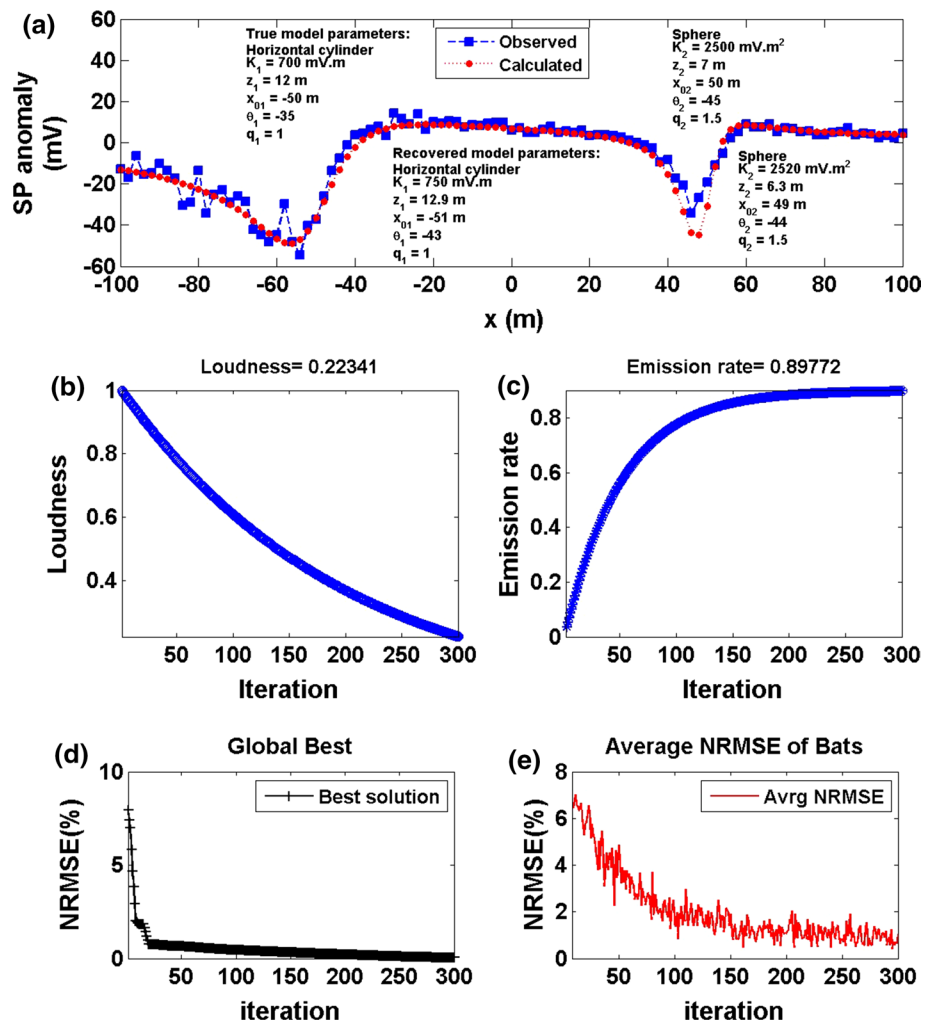


Table 2 Model– 1: True and recovered model parameters of the noisy composite interference SP anomaly of a horizontal cylinder and a sphere model (20% random Gaussian noise) with corresponding RE for each model parameters using the BOA

| Model parameters | True value | | Search range | Recovered value | | RE (%) | | O_{Fn} |
|-----------------------|---------------------------|--------------|--------------|---------------------------|------------------|---------------------------|--------------|-----------------|
| | Horizontal cylinder model | Sphere model | | Horizontal cylinder model | Sphere model | Horizontal cylinder model | Sphere model | |
| K ($mV.m^{2q-1}$) | 700 | 2500 | 100:3000 | 750 ± 60.39 | 2520 ± 59.90 | 7.14 | 0.80 | $1.0 * 10^{-7}$ |
| z (m) | 12 | 7 | 1:15 | 12.9 ± 0.96 | 6.3 ± 0.91 | 7.50 | 10.00 | |
| x_o (m) | -50 | 50 | -100:100 | -51 ± 0.65 | 49 ± 0.65 | 2.00 | 2.00 | |
| θ ($^\circ$) | -35 | -45 | -5:-90 | -43 ± 5.95 | -44 ± 6.00 | 22.86 | 2.22 | |
| q | 1 | 1.5 | 0.5:1.5 | 1 ± 0.40 | 1.5 ± 0.25 | 0 | 0 | |

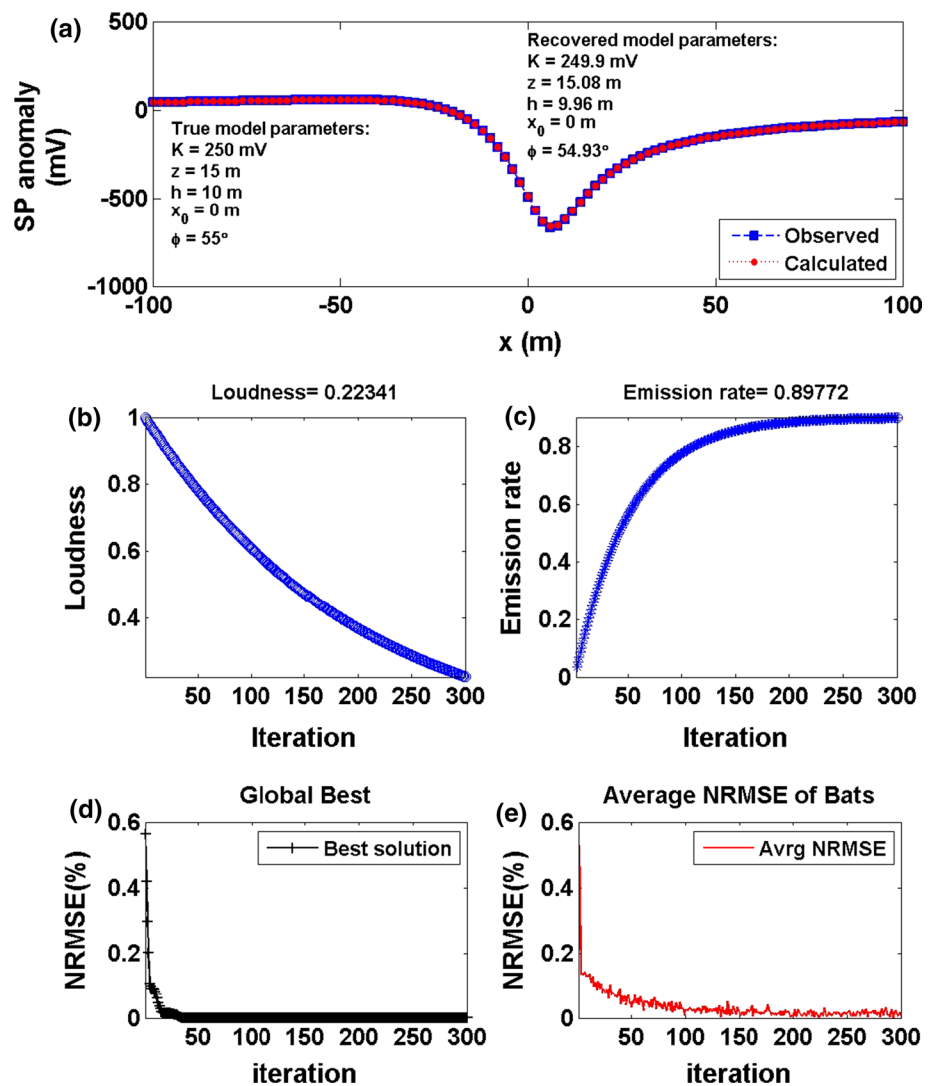
composite anomaly and the recovered model parameters of the two introduced models after noise contamination differ slightly from the true ones. The RE and SD of the recovered parameters are illustrated in Table 2. Generally, the parameters recovered using the BOA algorithm for the noisy interference sources are in great matching with the

true ones (Table 2). The obtained results support and confirm the mentioned BOA algorithm finding.

Model-2: 2D inclined sheet

To further investigate the BOA algorithm for studying the geological structures, such as faults, a noise-free example

Fig. 7 Model 2: noise-free synthetic example of the inclined sheet model. **a** The measured SP anomaly generated by inclined sheet model (true model parameters), as well as the calculated SP response (recovered model parameters) using the BOA, **b** loudness of the bats, **c** emission rate of the bats, **d** NRMSE of the global best solution (O_{Fn}) of the bats, and **e** the average NRMSE of all the bats



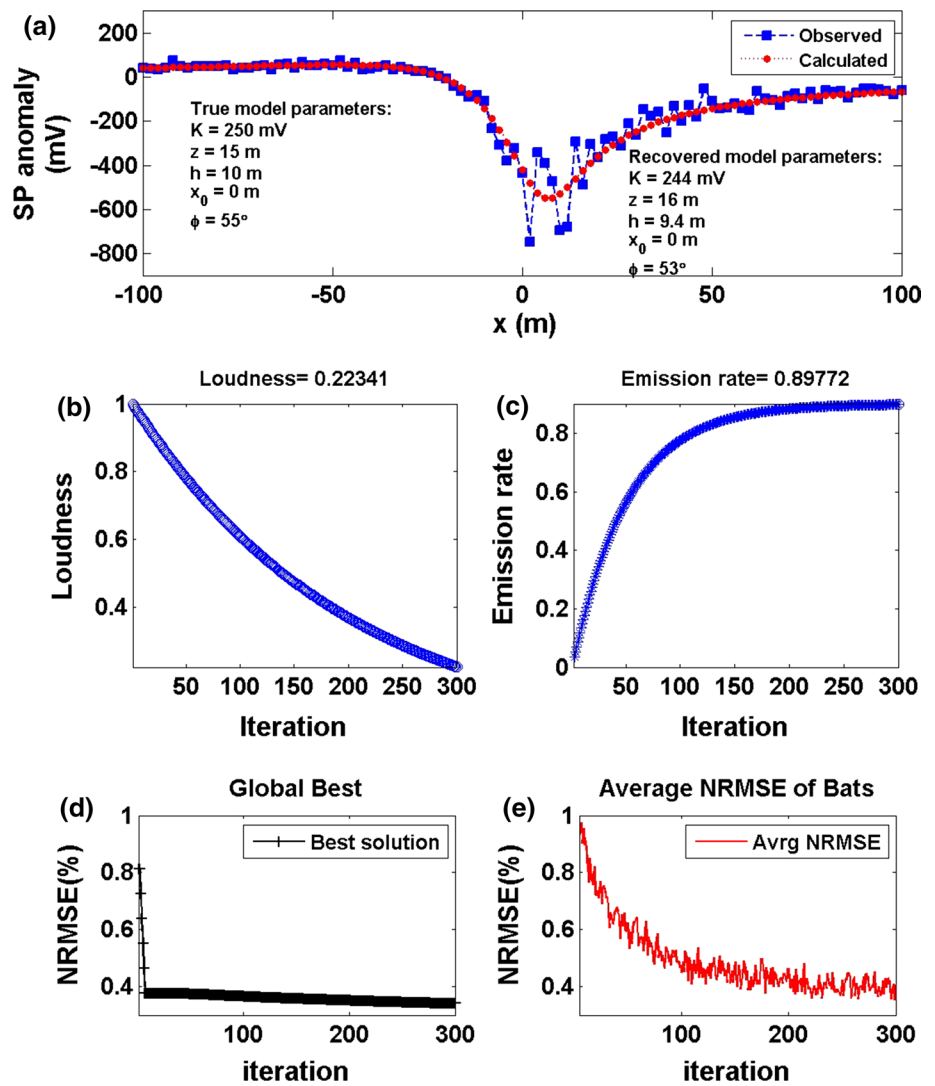
of a 2D inclined sheet model has been examined (model d in Fig. 2). The SP effect of the 2D inclined sheet model with input parameters: $K = 250$ mV, $z = 15$ m, $h = 10$ m, $x_0 = 0$ m and $\phi = 55^\circ$ is calculated using Eq. (8) of the inclined sheet model with a 200-m-long profile (Fig. 7a). Applying the same procedure of the BOA algorithm described above, the computed SP response of the 2D inclined sheet model is displayed in Fig. 7a. The average loudness of the SP anomaly is revealed in Fig. 7b, and the emission rate of the bat is obtained in Fig. 7c. The

NRMSE of the global best solution (min objective function, O_{Fn}) is shown in Fig. 7d, and the average NRMSE of all the bats is shown in Fig. 7e. Figure 7a and Table 3 show that the recovered model parameters of the 2-D inclined sheet model are identical to the true one. The RE and SD of the recovered parameters are illustrated in Table 3. The result supports that the BOA algorithm can be used to investigate the geological structure like sheets or faults, precisely.

Table 3 Model-2: True and recovered model parameters of the noise-free synthetic example of the inclined sheet with the corresponding RE for each parameter using the BOA

| Model parameters | True value | Search range | Recovered value | RE (%) | O_{Fn} |
|---------------------|------------|--------------|--------------------|--------|-----------------|
| K (mV) | 250 | 50:500 | 249.90 ± 0.064 | 0.04 | $6.0 * 10^{-9}$ |
| z (m) | 15 | 5:25 | 15.08 ± 0.062 | 0.53 | |
| h (m) | 10 | 1:15 | 9.96 ± 0.060 | 0.40 | |
| x_0 (m) | 0 | -100:100 | 0.00 ± 1.632 | 0.00 | |
| ϕ ($^\circ$) | 55 | 5:90 | 54.93 ± 0.05 | 0.13 | |

Fig. 8 Model 2: noisy synthetic example of the inclined sheet model. **a** The measured SP anomaly generated by inclined sheet model in Fig. 7a after adding 20% random Gaussian noise to the data (true model parameters), as well as the calculated SP response (recovered model parameters) using the BOA, **b** loudness of the bats, **c** emission rate of the bats, **d** NRMSE of the global best solution (O_{Fn}) of the bats, and **e** the average NRMSE of all the bats



The stability of the BOA algorithm is tested on the inclined sheet model by introducing a 20% Gaussian noise to the SP effect presented in Fig. 7a. Using the same procedures of the BOA algorithm to the noisy data, the best model parameter recovered at the minimum NRMSE of the objective functions (O_{Fn}). Figure 8a shows the contaminated SP anomaly after adding the 20% noise and the calculated SP response after obtaining the best model parameters using the BOA inversion algorithm. The loudness and emission rate of the bats are shown in Fig. 8b, c. Figure 8d, e depicts the

NRMSE of the global best solution (min objective function, O_{Fn}) and the average NRMSE of all the bats. Table 4 shows that the recovered model parameters of the contaminated self-potential anomaly are not significantly affected by the noise and are too close to the actual ones. Therefore, it can be concluded that the BOA algorithm suggested here is stabilized with regard to noise. The RE and SD of the recovered model parameters are illustrated in Table 4.

Table 4 Model-2: True and recovered model parameters of the noisy synthetic example of the inclined sheet after adding 20% random Gaussian noise to the SP anomaly and the corresponding RE for each parameter using the BOA

| Model parameters | True value | Search range | Recovered value | RE (%) | O_{Fn} |
|------------------|------------|--------------|-----------------|--------|-----------------|
| K (mV) | 250 | 50:500 | 244 ± 6.84 | 2.40 | $1.0 * 10^{-6}$ |
| z (m) | 15 | 5:25 | 16 ± 0.81 | 6.66 | |
| h (m) | 10 | 1:15 | 9.4 ± 0.68 | 6.00 | |
| x_o (m) | 0 | -100:100 | 0.01 ± 3.23 | 0.00 | |
| ϕ (°) | 55 | 5:90 | 53 ± 6.83 | 3.63 | |

Field datasets test

In the following sections, we studied the application of the developed BOA to three published SP field datasets for mineral exploration and geological structure investigation. The first example is the KTB anomaly (multiple-sources anomaly) from Germany for graphite deposits exploration. The second example is the Pinggirsari anomaly from Indonesia for delineating fault structure. Finally, the third example is the Bavarian woods graphite deposits anomaly (Germany) investigation.

The KTB SP anomaly, Germany

The KTB SP anomaly was observed around KTB-Boreholes through the Continental Deep Drilling Program in the north sector of Oberpfalz, northeast of Bavaria, Germany (Stoll et al. 1995) (Fig. 9). Two distinct negative peak anomaly zones are visible in this anomaly. The location of these two distinct peak anomalies should be the appropriate position of the subsurface structure. The graphite deposits found on the KTB's shear faults are only a few meters in thicknesses (Stoll et al. 1995). Graphite mineralization was the primary source of strong electrical conductivities in the upper crust (Stoll et al. 1995; Biswas 2017). Boreholes was conducted at the KTB-VB to 4 km in depth, and at KTB-HB to 200 m distant and around 9.1 km in depth (Emmermann and Lauterjung

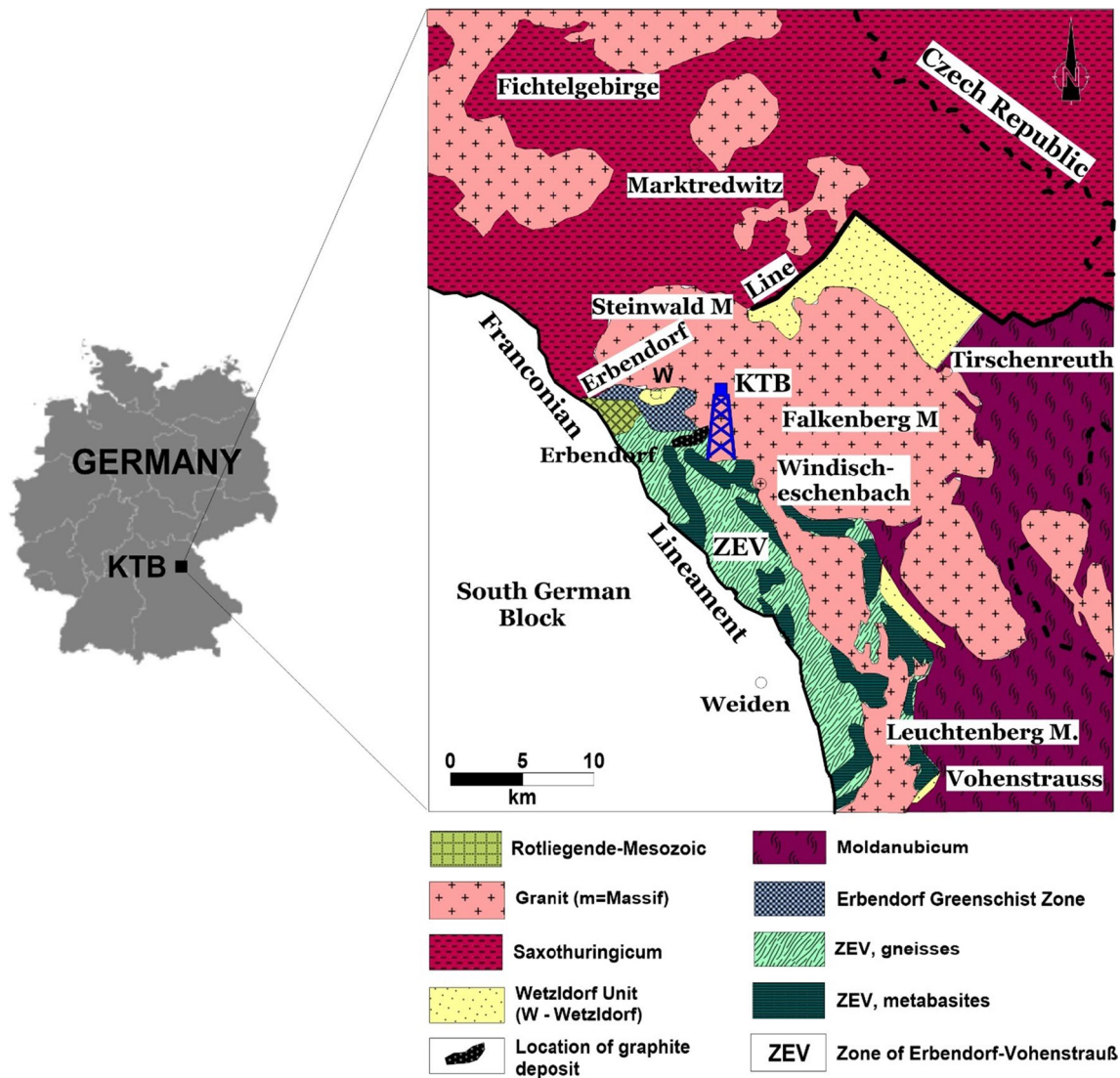
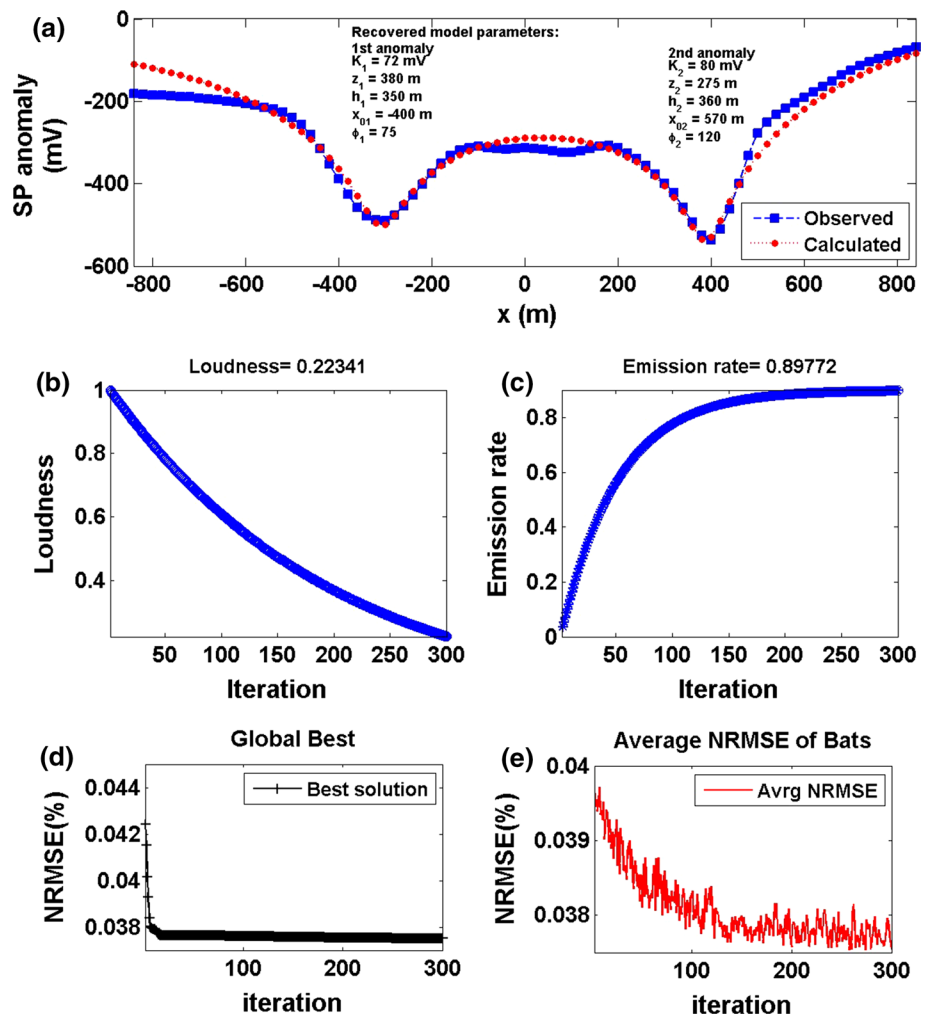


Fig. 9 Geological map in the vicinity KTB area, northern Oberpfalz, Germany (modified after Stoll et al. 1995; Hirschmann et al. 1997)

Fig. 10 KTB SP anomaly, Germany. **a** The measured SP anomaly profile (blue squares), and the calculated best-fitting SP response (red circles) using the BOA, **b** loudness of the bats, **c** emission rate of the bats, **d** NRMSE of the global best solution (O_{Fn}) of the bats versus the iteration numbers, and **e** the average NRMSE of all the bats



1997). The KTB SP anomaly is digitized at a 20 m sampling interval (Fig. 10a).

The KTB SP anomaly is investigated by different techniques (Stoll et al. 1995; Srivastava and Agarwal 2009; Mehane 2015; Biswas 2017; Sungkono 2020). Stoll et al. (1995) interpreted the SP anomaly of KTB using electrochemical modeling method with depths at 50 m and 30 m. Srivastava and Agarwal (2009) interpreted the SP anomaly employing the ELW approach considering quasi-sheet-like structures with depths at 135.5 m and 80 m. Mehane (2015) analyzed the anomaly exploiting deterministic inversion in

view of thin sheet-type structures with depths about 27 m and 26 m to the top of the sheet structures. Biswas (2017) reinterpreted the KTB anomaly utilizing the VFSA global optimization technique takes into accounting thin sheet-type structure with depths 372 m and 298 m to the center of the sheet structures. Sungkono (2020) interpreted the anomaly using micro-differential evolution (including MVDE and μ JADE) technique as thin sheet type structures with depths to the center at 447.09 m and 134.82 m using MVDE and using μ JADE with depths to the center at 556.99 m and 154.15 m.

Table 5 KTB self-potential anomaly, Germany. Recovered model parameters with the corresponding min O_{Fn} for each parameter using the BOA

| Model parameters | Search range | Recovered value | | O_{Fn} |
|------------------|--------------|------------------|-----------------|-----------------|
| | | First anomaly | Second anomaly | |
| K (mV) | 1:150 | 72 ± 16.90 | 80 ± 31.61 | $1.0 * 10^{-6}$ |
| z (m) | 1:500 | 380 ± 11.47 | 275 ± 68.32 | |
| h (m) | 1:500 | 350 ± 43.11 | 360 ± 59.99 | |
| x_o (m) | -850:850 | -400 ± 46.60 | 570 ± 47.80 | |
| ϕ (°) | 5:180 | 75 ± 16.56 | 120 ± 25.81 | |

The KTB SP anomaly is interpreted using the presented BOA algorithm considering thin sheet-type structures. Applying the procedures of the BOA algorithm discussed before, the characteristics source parameters of the KTB SP anomaly were estimated (Table 5). Figure 10b, c shows the average loudness and emission rate of the bat over the self-potential anomaly, respectively. Figure 10d, e shows the NRMSE of the global best solution (min objective function, O_{Fn}) and the average NRMSE of all the bats, respectively. The best-interpreted model parameters occurred at the min NRMSE of the O_{Fn} . The min O_{Fn} is 0.000001 and the corresponding inferred model parameters of the first anomaly are $K_1 = 72$ mV, $z_2 = 380$ m, $x_{o1} = -400$ m, $h_1 = 350$ m, and $\varphi_1 = 75^\circ$, while the best-inferred characteristic parameters of the second anomaly are $K_2 = 80$ mV, $z_2 = 375$ m, $x_{o2} = 570$ m, $h_2 = 360$ m, and $\varphi_2 = 120^\circ$ (Table 5). The depths obtained here are in good agreement with those obtained by Biswas (2017) and Sungkono (2020). The observed and calculated self-potential KTB anomalies are extremely well matched (Fig. 10a). Table 6 displays a comparison of the outcomes introduced by the previous methods and the obtained results using the proposed BOA algorithm. Figure 11 shows the sketch diagram of the results obtained by Stoll et al. (1995) using the trial-and-error technique (Fig. 11a) and the present approach (Fig. 11b). According to these results, the present approach gives a more insight view with the geological cross-section (Fig. 11c) for the KTB anomaly than Stoll et al. (1995).

The Pinggirsari SP anomaly, Indonesia

The SP anomaly of Pinggirsari is observed to identify and characterize the fault structure in the Pinggirsari village, Java, Indonesia (Fajriani et al. 2017). The data acquisition of the self-potential has been intersected the fault location in the study area as displayed in the geological map (Fig. 12 top panel), while the geological cross section was taken in S–N direction parallel to the SP survey line and perpendicular to the fault strike along the geological map to show the structure variation perfectly (Fig. 12 lower panel). The observed

SP data were smoothed employing the moving average filter to sharpen the anomaly of SP and eliminate the regional background effects. The SP anomaly shows the occurrence of high potential difference anomalous with value of about 162 mV located at a distance between 400 and 600 m. A 10-m sample interval is utilized to digitize the Pinggirsari self-potential anomaly of 1040 m length (Fig. 13a).

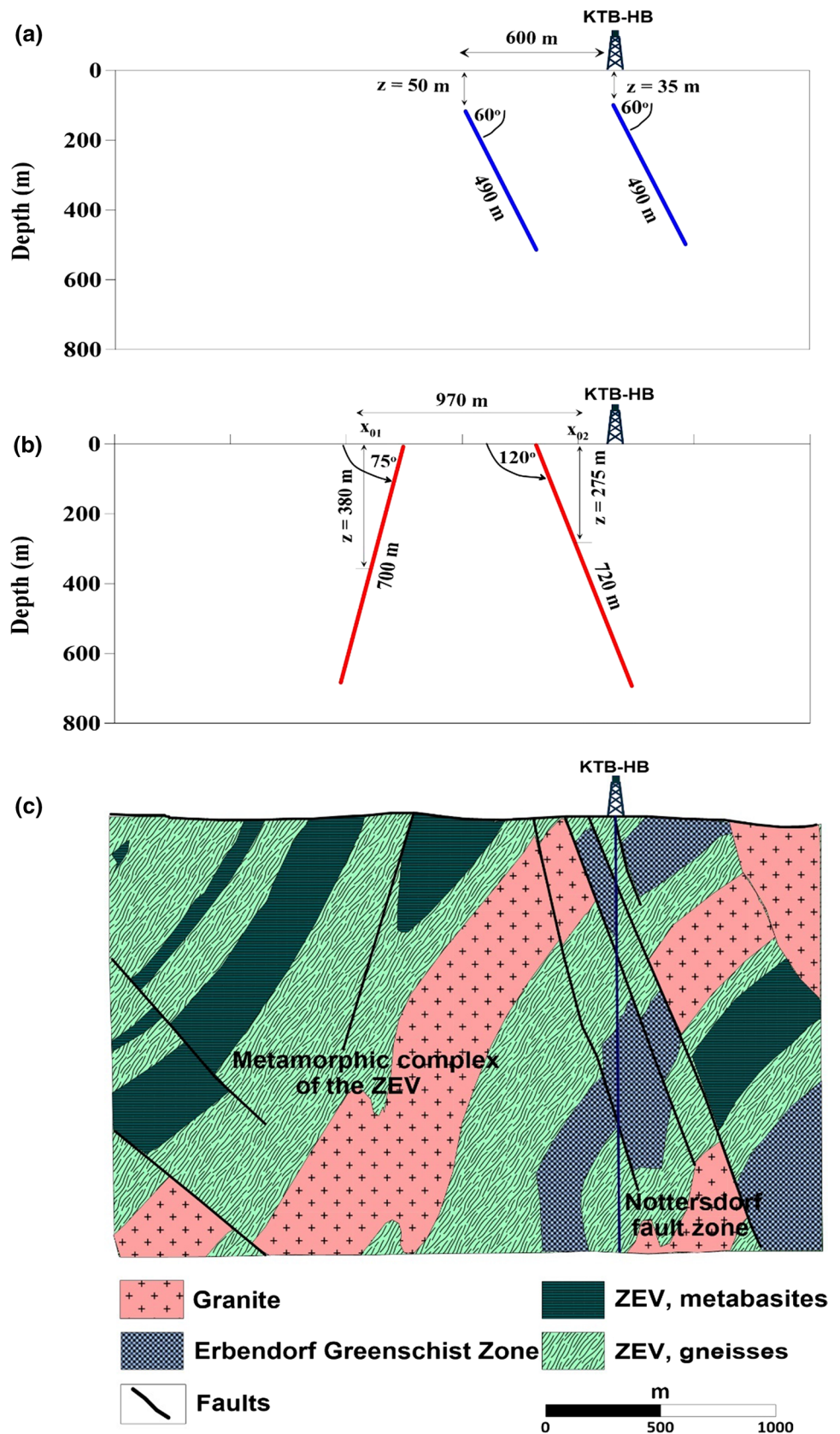
The SP anomaly of Pinggirsari is interpreted by applying the BOA. The characteristics source parameters of the Pinggirsari SP anomaly can be estimated (Table 7). Figure 13b, c shows the average loudness and emission rate of the bat over the SP anomaly, respectively. Figure 13d, e shows the NRMSE of global best solution and the average NRMSE of all the bats, correspondingly. The best-interpreted model parameters are $K = 51$ mV, $z = 16$ m, $x_o = 5$ m, $h = 43$ m, and $\varphi = 223^\circ$, which suggests that the effect of the SP anomaly resulted from a thin sheet-like model approximated by fault structure (Table 7). The observed and calculated self-potential anomalies are well matched (Fig. 13a).

The observed SP anomaly of Pinggirsari has been explored by different authors researchers. For example, Fajriani et al. (2017) interpret the SP anomaly as a thin sheet (i.e., approximated by fault) using the Levenberg–Marquardt (LM) method with depth to the center $z = 14.63$ m. Haryono et al. (2020) interpret the SP anomaly as a 2D inclined sheet (approximately fault) using the improved crow search algorithm (ICSA) technique with top depth $z_1 = 7.15$ m and bottom depth $z_2 = 32.79$ m. Sungkono (2020) analyzed the Pinggirsari SP anomaly using the micro-differential evolution method, which included two approaches [the vectorized random mutation factor (MVDE) and the adaptive differential evolution (μ JADE)]. The depth to the center using the MVDE approach was 20 m, while the depth determined by the μ JADE approach was 19.55 m. The obtained depth of the developed BOA algorithm here is to the center of the 2D inclined thin sheet, approximated by fault structure. The orientation and the depth of the fault structure, as shown in Table 8, are in good accordance with the published literature and geological cross-sectional information. Figure 14 shows

Table 6 Comparison results of the KTB SP anomaly, Germany

| Algorithm | Source | K (mV) | z (m) | h (m) | x_o (m) | φ ($^\circ$) |
|----------------------------|------------|----------------|-----------------|-----------------|------------------|------------------------|
| VFSA (Biswas 2017) | Anomaly #1 | 73.5 | 371.8 | 524.6 | 998.6 | 139.6 |
| | Anomaly #2 | 79.0 | 298.2 | 394.8 | 1472.1 | 134.2 |
| MVDE (Sungkono 2020) | Anomaly #1 | 74.98 | 447.09 | 429.13 | 505.52 | 79.11 |
| | Anomaly #2 | 120.06 | 134.82 | 128.86 | 1224.99 | 103.95 |
| μ JADE (Sungkono 2020) | Anomaly #1 | 67.08 | 556.99 | 530.23 | 500.00 | 80.00 |
| | Anomaly #2 | 91.67 | 154.15 | 149.84 | 1271.08 | 117.76 |
| BOA (Present study) | Anomaly #1 | 72 ± 16.90 | 380 ± 11.47 | 350 ± 43.11 | -400 ± 46.60 | 75 ± 16.56 |
| | Anomaly #2 | 80 ± 31.61 | 275 ± 68.32 | 360 ± 59.99 | 570 ± 47.80 | 120 ± 25.81 |

Fig. 11 **a** Sketch diagram for the results obtained by Stoll et al. (1995) using trial and error modeling, **b** The interpreted sketch diagram using the developed BOA for the KTB anomaly, **c** Geological cross-section in the vicinity of the KTB-HB borehole, Germany. (modified after Stoll et al. 1995)



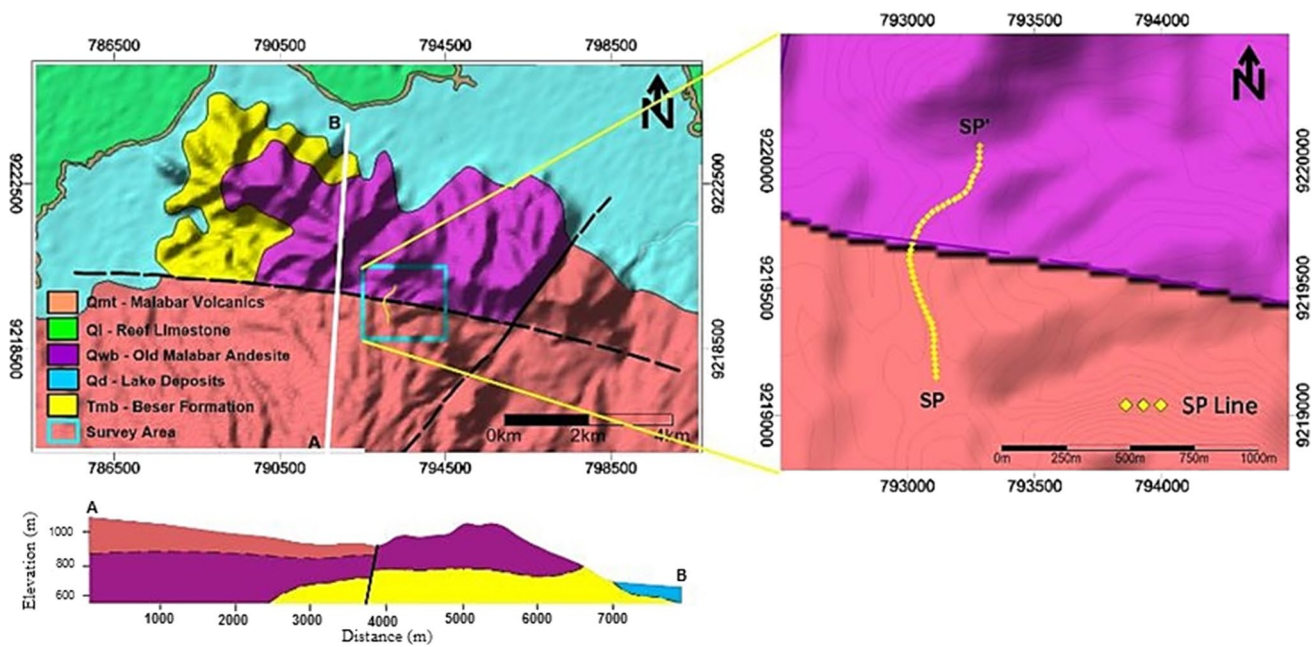


Fig. 12 Pinggirsari area location showing the measurement of SP data represented by SP line, geological map of the surrounded area (upper panel) (note the presence of fault outcrop on the surface of

the geological map) and cross-section AB from the geological map crossed the fault (lower panel) (modified after Alzwar et al. 1992; Fajriani et al. 2017)

the interpreted designed graph of the buried source structure outlined employing the BOA method.

The bavarian woods SP anomaly, Germany

The SP anomaly gathered across a graphite ore body in the southern Bavarian woods in Germany is outlined in Fig. 15a (Meiser 1962). The graphite deposits are wedged amongst crystalline limestone and paragneiss of similar age in a Hercynian gneissic complex. Typically, the ore deposit produces creases that are classified as Precambrian bituminous sediments. The veins of the graphite are therefore wedged through the gneisses and limestone, forming a parallel series of thickness-inconsistent lenses (Meiser, 1962). A 5.2-m sample interval is exploited to digitize the SP anomaly profile with length of 525 m (Fig. 15a).

The Bavarian Wood anomaly has been examined by various researchers. Al-Garani (2010) interpreted the SP anomaly approximately as a horizontal cylindrical target applying the neural network (NN) inversion with $z = 33$ m. Mehanee (2014) interpreted the SP anomaly profile employing the regularized inversion technique as a horizontal cylindrical model with a depth to the center equals 46 m. Göktürkler and Balkaya (2012) using the genetic algorithm described the SP anomaly by a horizontal cylinder model ($z = 45.03$ m), simulated annealing ($z = 47.59$ m), and a particle swarm algorithm ($z = 47.59$ m). Di Maio et al. (2016) match the SP

Bavarian anomaly by a horizontal cylinder using a spectral analysis and tomographic approach with depth of 44.9 m. Essa (2020) utilized the particle swarm optimization (PSO) technique and interpreted the Bavarian wood anomaly with depth of 51.6 m.

We interpreted the SP anomaly of the Bavarian wood using the present BOA method. The BOA interpretation procedures have been applied to the SP anomaly profile using a suitable search range for the characteristics source parameters (Table 9). Figure 15b, c presents the average loudness and emission rate of the bat over the SP anomaly, respectively. Figure 15d, e represents the NRMSE of global best solution and the average NRMSE of all the bats, respectively. The best interpretative model parameters are $K = 29,000$ mV.m, $z = 49$ m, $x_0 = 5$ m, $q = 1$ and $\theta = -55^\circ$, which suggests that the ore deposit body is approximated by a horizontal cylinder-like model (Table 9). The observed anomaly of the Bavarian as well as the calculated anomaly is matched very well as shown in Fig. 15a. The depth of burial (z) as shown in Table 10 is in excellent accordance with the scholarly works. Figure 16 shows the interpreted designed graph of the buried source structure outlined from the BOA (Fig. 16a) and geological cross section (Meiser 1962) (Fig. 16b).

Fig. 13 Pinggirsari SP anomaly, Indonesia. **a** The measured SP anomaly profile (blue squares), and the calculated best-fitting SP response (red circles) using the BOA, **b** loudness of the bats, **c** emission rate of the bats, **d** NRMSE of the global best solution (O_{Fn}) of the bats versus the iteration numbers, and **e** the average NRMSE of all the bats

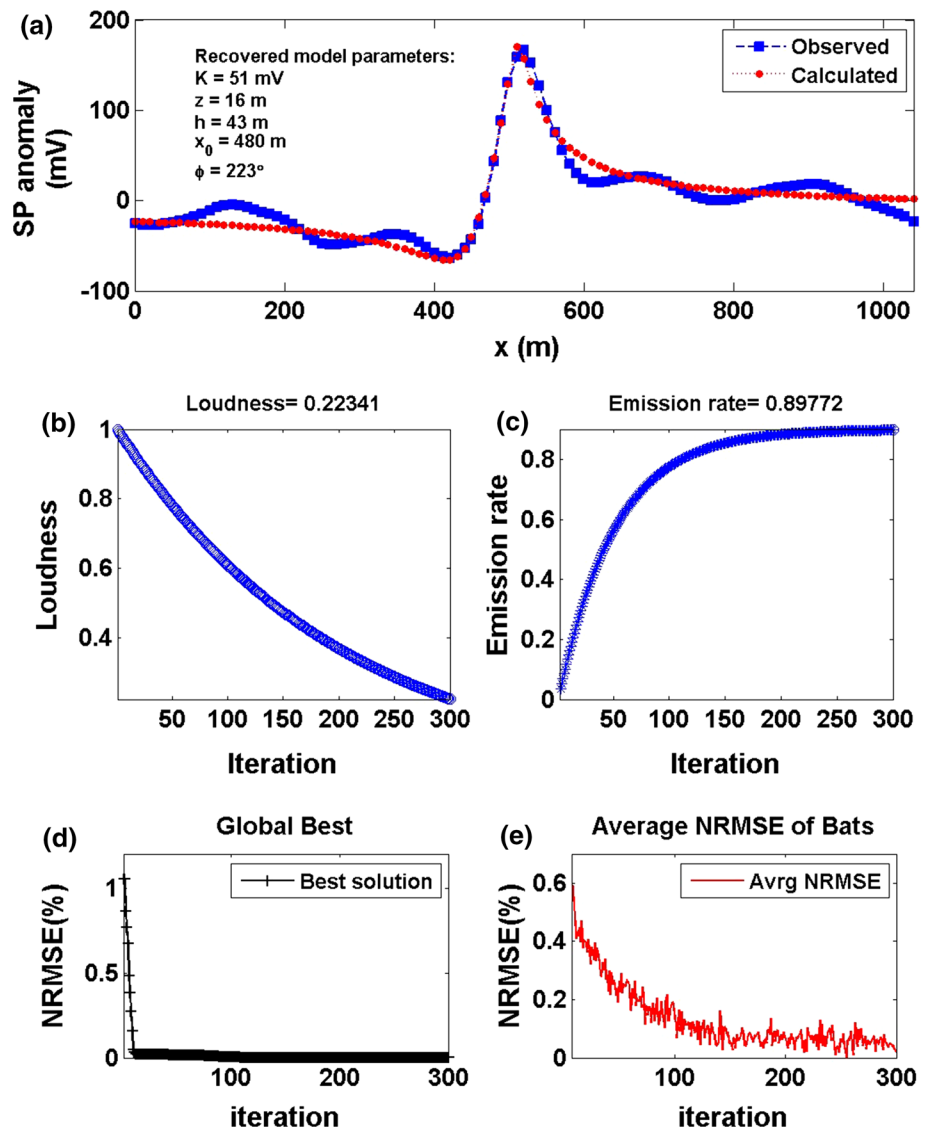


Table 7 Pinggirsari SP anomaly, Indonesia. Recovered model parameters with the corresponding min O_{Fn} for each parameter using the BOA

| Model parameters | Search range | Recovered value | O_{Fn} |
|---------------------|--------------|-----------------|-----------------|
| K (mV) | 1:200 | 51 ± 3.26 | $1.8 * 10^{-5}$ |
| z (m) | 1:100 | 16 ± 2.44 | |
| h (m) | 10:200 | 43 ± 1.63 | |
| x_0 (m) | -262:262 | 480 ± 77.0 | |
| ϕ ($^\circ$) | 5:360 | 223 ± 3.27 | |

Table 8 Comparison results of the Pinggirsari SP anomaly, Indonesia

| Model parameters | Fajriani et al. (2017) | Sungkono (2020) | | Present Study |
|---------------------|------------------------|-----------------|------------|----------------|
| | | MVDE | μ JADE | |
| K (mV) | 41.5 | 48.67 | 46.85 | 51 ± 3.26 |
| z (m) | 14.63 | 20.00 | 19.55 | 16 ± 2.44 |
| h (m) | 34 | 31.72 | 33.01 | 43 ± 1.63 |
| x_0 (m) | 478.25 | 481.01 | 480.07 | 480 ± 77.0 |
| ϕ ($^\circ$) | 334.52 | -156.20 | -156.93 | 223 ± 3.27 |

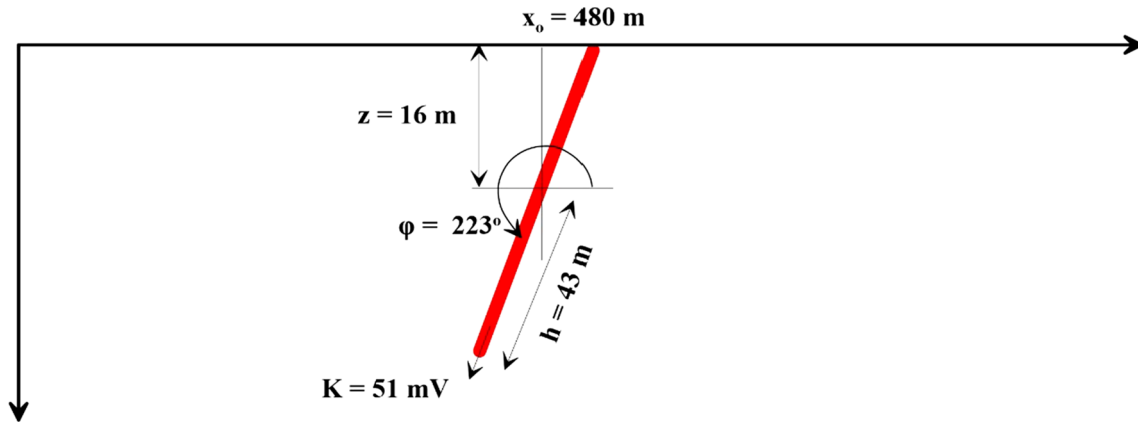


Fig. 14 Sketch diagrams show the buried source of the SP anomaly of Pinggirsari outlined from the suggested BOA

Fig. 15 Bavarian wood SP anomaly, Germany. **a** The measured SP anomaly profile (blue squares) and the calculated best-fitting SP response (red circles) using the BOA, **b** loudness of the bats, **c** emission rate of the bats, **d** NRMSE of the global best solution (O_{FB}) of the bats versus the iteration numbers, and **e** the average NRMSE of all the bats

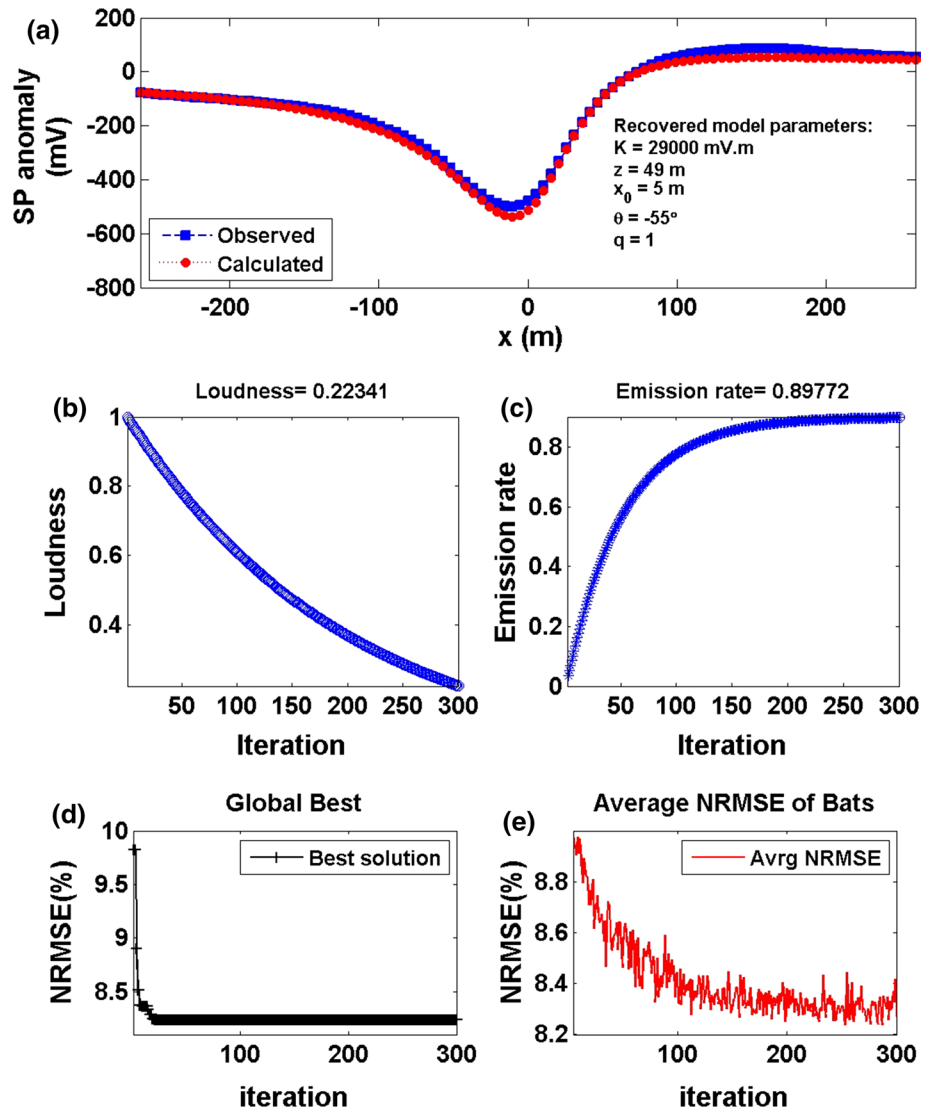


Table 9 Bavarian wood SP anomaly, Germany. Recovered model parameters with the corresponding min O_{Fn} for each parameter using the BOA

| Model parameters | Search range | Recovered value | O_{Fn} |
|------------------|---------------|-------------------|-----------------|
| K (mV.m) | 10,000:50,000 | $29,000 \pm 1581$ | $1.0 * 10^{-5}$ |
| z (m) | 1:100 | 49 ± 5.99 | |
| x_o (m) | -262:262 | 5 ± 2.16 | |
| θ (°) | -5:-90 | -55 ± 6.00 | |
| q | 0.5:1.5 | 1 ± 0.40 | |

Conclusions

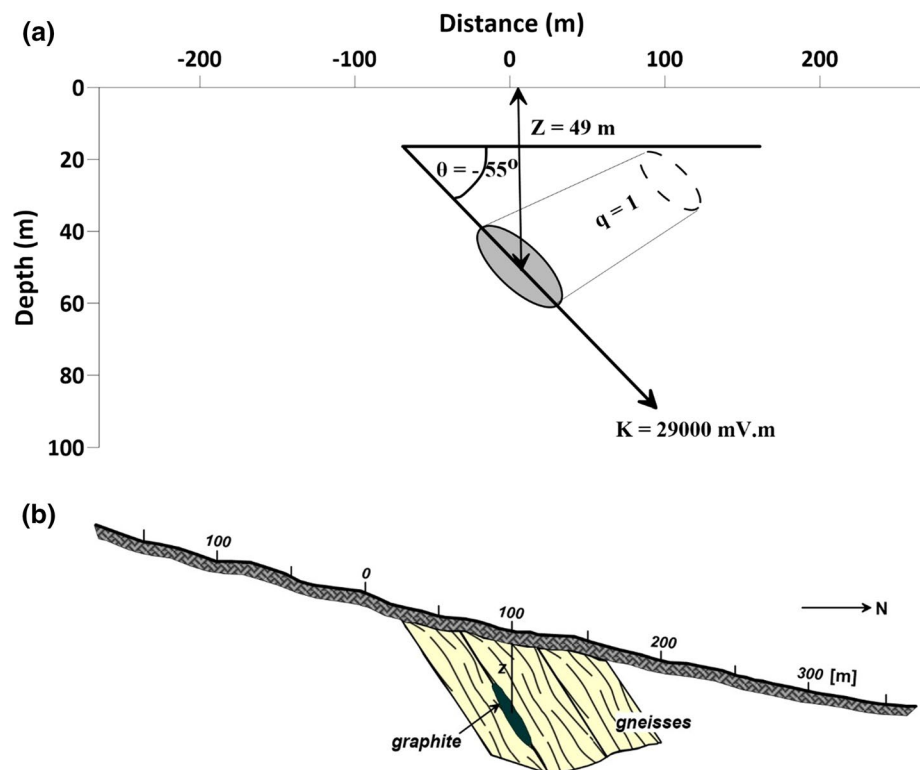
We have introduced a global optimization metaheuristic algorithm so-called Bat optimization algorithm (BOA)

with an application to interpret the SP data for obtaining the best convenient characteristic parameters and discover a satisfactory buried model. The best-interpreted model parameters are obtained corresponding to the minimum objective function after reaching the global best solution. The BOA method does not require a priori information; the recovered solutions depend on using a search space to search for the model parameters which is controlled by the NRMS of the objective function. The benefits of the BOA method can handle multi-model problems efficiently. Furthermore, the appropriate efficiency and accuracy of the suggested method have been confirmed on numerical datasets with noise-free and noise. In addition to, the BOA method is verified on various real datasets with fruitful results compared to the drilling and geological information. At the end, we recommend the proposed method

Table 10 Comparison results of the Bavarian wood SP anomaly, Germany

| Model parameters | Essa et al. (2008) | Essa (2011) | Göktürkler GA | And PSO | Balkaya (2012) SA | Mehanee (2014) | Di Maio et al. (2016) | Present Study |
|------------------|--------------------|-------------|---------------|----------|-------------------|----------------|-----------------------|-------------------|
| K (mV.m) | 30,608.7 | 27,212.7 | 21,272.9 | 33,343.8 | 26,257.4 | 27,105 | 25,000 | $29,000 \pm 1581$ |
| z_o (m) | 47.7 | 46.59 | 45.03 | 47.59 | 44.99 | 46 | 44.9 | 49 ± 5.99 |
| x_o (m) | – | – | 268.79 | 269.88 | 269.17 | – | 265.9 | 5 ± 2.16 |
| θ (°) | -51.2 | -59.04 | -51.29 | -48.6 | -49.98 | -57 | -59.5 | -55 ± 6.00 |
| q | 1.0 | 1.0 | 1.0 | 1.0 | 1.0 | 1.0 | 1.0 | 1.0 ± 0.40 |

Fig. 16 **a** A sketch diagram for the buried source model outlined using the BOA, and **b** geological cross section (after Meiser 1962)



extended to be applied in the future to investigate different potential field data.

Acknowledgements Authors would like to thank Prof. Dr. Eleftheria E. Papadimitriou, Editor-in-Chief, Prof. Dr. Bogdan Mihai Niculescu, Associate Editor, and the two reviewers for their keen interest, valuable comments on the manuscript, and improvements to this work.

Funding Open access funding provided by The Science, Technology & Innovation Funding Authority (STDF) in cooperation with The Egyptian Knowledge Bank (EKB).

Declarations

Conflict of interest Authors declare that there are no conflicts of interest to this work.

Open Access This article is licensed under a Creative Commons Attribution 4.0 International License, which permits use, sharing, adaptation, distribution and reproduction in any medium or format, as long as you give appropriate credit to the original author(s) and the source, provide a link to the Creative Commons licence, and indicate if changes were made. The images or other third party material in this article are included in the article's Creative Commons licence, unless indicated otherwise in a credit line to the material. If material is not included in the article's Creative Commons licence and your intended use is not permitted by statutory regulation or exceeds the permitted use, you will need to obtain permission directly from the copyright holder. To view a copy of this licence, visit <http://creativecommons.org/licenses/by/4.0/>.

References

- Abdelrahman EM, Saber HS, Essa KS, Fouda MA (2004) A least-squares approach to depth determination from numerical horizontal self-potential gradients. *Pure Appl Geophys* 161:399–411
- Abdelrahman EM, Essa KS, Abo-Ezz ER, Soliman KS (2006) Self-potential data interpretation using standard deviations of depths computed from moving average residual anomalies. *Geophys Prospect* 54:409–423
- Abdelrahman EM, El-Araby TM, Essa KS (2009) Shape and depth determinations from second moving average residual self-potential anomalies. *J Geophys Eng* 6:43–52
- Al-Garani MA (2010) Interpretation of spontaneous potential anomalies from some simple geometrically shaped bodies using neural network inversion. *Acta Geophys* 58:143–162
- Alzwar M, Akbar N, Bachri S (1992) Geological Map of Garut and Pameungpeuk sheet, Jawa, Scale 1: 100,000. 2nd edn, Geological survey Centre, Geology Agency, Bandung
- Banerjee B (1971) Quantitative interpretation of self-potential anomalies of some specific geometric bodies. *Pure Appl Geophys* 90:138–152
- Biswas A (2017) A review on modeling, inversion and interpretation of self-potential in mineral exploration and tracing paleo-shear zones. *Ore Geol Rev* 91:21–56
- Biswas A, Mandal A, Sharma SP, Mohanty WK (2014) Delineation of subsurface structure using self-potential, gravity and resistivity surveys from south Purulia Shear zone, India: implication to uranium mineralization. *Interpretation* 2:T103–T110
- Di Maio R, Piegari E, Rani P, Avella A (2016) Self-Potential data inversion through the integration of spectral analysis and tomographic approaches. *Geophys J Int* 206:204–220
- Di Maio R, Piegari E, Rani P (2017) Source depth estimation of self-potential anomalies by spectral methods. *J Appl Geophys* 136:315–325
- Di Maio R, Piegari E, Rani P, Carbonari R, Vitagliano E, Milano L (2019) Quantitative interpretation of multiple self-potential anomaly sources by a global optimization approach. *J Appl Geophys* 162:152–163
- Drahor MG (2004) Application of the self-potential method to archaeological prospection: some case histories. *Archaeol Prospect* 11:77–105
- Elhussein M (2021) A novel approach to self-potential data interpretation in support of mineral resource development. *Nat Resour Res* 30:97–127
- Emmermann R, Lauterjung J (1997) The German continental deep drilling program KTB: overview and major results. *J Geophys Res-Solid Earth* 102(B8):18179–18201
- Eppelbaum LV (2021) Review of processing and interpretation of self-potential anomalies: transfer of methodologies developed in magnetic prospecting. *Geosciences* 11:194
- Essa KS (2011) A new algorithm for gravity or self-potential data interpretation. *J Geophys Eng* 8:434–446
- Essa KS (2019) A particle swarm optimization method for interpreting self-potential anomalies. *J Geophys Eng* 16:463–477
- Essa KS (2020) Self potential data interpretation utilizing the particle swarm method for the finite 2D inclined dike: mineralized zones delineation. *Acta Geod Geophys* 55:203–221
- Essa KS, Diab ZE (2022) Source parameters estimation from gravity data using bat algorithm with application to geothermal and volcanic activity. *Int J Environ Sci Technol*. <https://doi.org/10.1007/s13762-022-04263-z>
- Essa KS, Elhussein M (2017) A new approach for the interpretation of self-potential data by 2-D inclined plate. *J Appl Geophys* 136:455–461
- Essa KS, Mahanee S, Smith PD (2008) A new inversion algorithm for estimating the best fitting parameters of some geometrically simple body to measured self-potential anomalies. *Explor Geophys* 39:155–163
- Essa KS, Diab ZE, Elhussein M (2020) Self-potential data interpretation for two co-axial structures utilizing the RMS Parameter. *J Environ Eng Geophys* 25:15–23
- Essa KS, Mehanee S (2007) A rapid algorithm for self-potential data inversion with application to mineral exploration, In: 19th International geophysical conference and exhibition, Australian society of exploration geophysicists, Perth, Australia
- Fajriani WS, Pratomo PM (2017) Interpretation of Self-Potential anomalies for investigating fault using the Levenberg-Marquardt method: a study case in Pinggirsari, West Java, Indonesia. *IOP Conf Ser: Earth Environ Sci* 62:012004. <https://doi.org/10.1088/1755-1315/62/1/012004>
- Fister IJ (2013) A comprehensive review of bat algorithms and their hybridization. M.Sc. thesis; University of Maribor, Slovenia
- Fister IJ, Fister I, Yang XS (2013) A Hybrid Bat Algorithm: *Electrotech Rev* 80:1–7
- Fournier C (1989) Spontaneous potentials and resistivity surveys applied to hydrogeology in a volcanic area: case history of the Chaîne des Puys (Puy-de-Dôme, France). *Geophys Prospect* 37:647–668
- Gao Y, Hao M, Wang Y, Dang L, Guo Y (2021) Multi-scale coal fire detection based on an improved active contour model from Landsat-8 satellite and UAV images. *ISPRS Int J Geo-Inf* 10:449
- Göktürkler G, Balkaya C (2012) Inversion of self-potential anomalies caused by simple geometry bodies using global optimization algorithms. *J Geophys Eng* 9:498–507
- Haryono A, Sungkono Agustin R, Santosa BJ, Widodo A, Ramadhany B (2020) Model parameter estimation and its uncertainty for 2-D

- inclined sheet structure in self-potential data using crow search algorithm. *Acta Geod Geophys* 55:691–715
- Heinze T, Limbrock JK, Pudasaini SP, Kemna A (2019) Relating mass movement with electrical self-potential signals. *Geophys J Int* 216:55–60
- Hirschmann G, Duyster J, Harms U, Kontny A, Lapp M, Hde W, Zulauf G (1997) The KTB superdeep borehole: petrography and structure of a 9-km-deep crustal section. *Geol Rundsch* 86:S3–S14
- Hunter L, Powers M (2008) Geophysical investigations of earthen dams: An overview. In: 21st SAGEEP, p 1083–1096
- Ikard SJ, Revil A, Jardani A, Woodruff WF, Parekh M, Mooney M (2012) Saline pulse test monitoring with the self-potential method to non-intrusively determine the velocity of the pore water in leaking areas of earth dams and embankments. *Water Resour Res* 48:W04201
- Kawada Y, Kasaya T (2018) Self-potential mapping using an autonomous underwater vehicle for the Sunrise deposit, Izu-Ogasawara arc, southern Japan. *Earth Planets Space* 70:142–156
- Khari M, Sinha A, Verdu E, Crespo RG (2020) Performance analysis of six meta-heuristic algorithms over automated test suite generation for path coverage-based optimization. *Soft Comput* 24:9143–9160
- Kukemilks K, Wagner J-F (2021) Detection of preferential water flow by electrical resistivity tomography and self-potential method. *Appl Sci* 11:4224
- Mehanee S (2014) An efficient regularized inversion approach for self-potential data interpretation of ore exploration using a mix of logarithmic and nonlogarithmic model parameters. *Ore Geol Rev* 57:87–115
- Mehanee S (2015) Tracing of paleo-shear zones by self-potential data inversion: case studies from the KTB, Rittsteig, and Grossensees graphite bearing fault planes. *Earth Planets Space* 67:14
- Mehanee SA (2021) Simultaneous joint inversion of gravity and self-potential data measured along profile: theory, numerical examples, and a case study from mineral exploration with cross validation from electromagnetic data. *IEEE Trans Geosci Remote Sens*. <https://doi.org/10.1109/TGRS.2021.3071973>
- Mehanee SA, Essa KS (2015) 2.5D regularized inversion for the interpretation of residual gravity data by a dipping thin sheet: numerical examples and case studies with an insight on sensitivity and non-uniqueness. *Earth, Planets Space* 67:130. <https://doi.org/10.1186/s40623-015-0283-2>
- Meiser P (1962) A method of quantitative interpretation of self-potential measurements. *Geophys Prospect* 10:203–218
- Minsley BJ, Sogade J, Morgan FD (2007) Three-dimensional self-potential inversion for subsurface DNAPL contaminant detection at the Savannah river site. *South Carolina Water Resour Res* 43:W04429
- Minsley BJ, Coles DA, Vichabian Y, Morgan FD (2008) Minimization of self-potential survey mis-ties acquired with multiple reference locations. *Geophysics* 73:F71–F81
- Oliveti I, Cardarelli E (2017) 2D approach for modeling self-potential anomalies: application to synthetic and real data. *Boll Geof Teor Appl* 58:415–430
- Pekşen E, Yas T, Kayman AY, Özkan C (2011) Application of particle swarm optimization on self-potential data. *J Appl Geophys* 75:305–318. <https://doi.org/10.1016/j.jappgeo.2011.07.0>
- Poormirzaee R, Sarmady S, Sharghi Y (2019) A new inversion method using a modified bat algorithm for analysis of seismic refraction data in dam site investigation. *JEEG* 24:201–214
- Poormirzaee R (2017) Applying bat metaheuristic algorithm for building shear wave velocity models from surface wave dispersion curves. In: 23rd European meeting of environmental and engineering geophysics, Sweden, p 1–5
- Rao AD, Babu RHV (1983) Quantitative interpretation of self potential anomalies due to two-dimensional sheet-like bodies. *Geophysics* 48:1659–1664
- Revil A, Jardani J, Dupont JP (2008) Reply to comment by D. Gibert and P. Sillhac on "Self-potential signals associated with preferential groundwater flow pathways in sinkholes". *J Geophys Res*. <https://doi.org/10.1029/2007JB005396>
- Rittgers JB, Revil A, Karaoulis M, Mooney MA, Slater LD, Atekwana EA (2013) Self-potential signals generated by the corrosion of buried metallic objects with application to contaminant plumes. *Geophysics* 78(5):EN65–EN82. <https://doi.org/10.1190/geo2013-0033.1>
- Santos FAM (2010) Inversion of self-potential of idealized bodies' anomalies using particle swarm optimization. *Comput Geosci* 36:1185–1190
- Shao Z, Wang D, Wang Y, Zhong X, Zhong Y, Song W (2017) Experimental study of the self-potential anomaly caused by coal fires. *J Appl Geophys* 145:124–132
- Sharma SP, Biswas A (2013) Interpretation of self-potential anomaly over a 2D inclined structure using very fast simulated-annealing global optimization—an insight about ambiguity. *Geophysics* 78(3):WB3–WB15
- Sharma SP, Kaikkonen P (1998) Two-dimensional non-linear inversion of VLF-R data using simulated annealing. *Geophys J Int* 133:649–668
- Sill WR (1983) Self-potential modeling from primary flows. *Geophysics* 48:76–86
- Soueid Ahmed A, Jardani A, Revil A, Dupont JP (2013) SP2DINV: A 2D forward and inverse code for streaming potential problems. *Comput Geosci* 59:9–16
- Soueid Ahmed A, Jardani A, Revil A, Dupont JP (2016) Specific storage and hydraulic conductivity tomography through the joint inversion of hydraulic heads and self-potential data. *Adv Water Resour* 89:80–90
- Srivastava S, Agarwal BNP (2009) Interpretation of self-potential anomalies by enhanced local wave number technique. *J Appl Geophys* 68:259–268
- Srivastava S, Datta D, Agarwal BN, Mehta S (2014) Applications of Ant Colony Optimization in determination of source parameters from total gradient of potential fields. *Near Surf Geophys* 12(3):373–390. <https://doi.org/10.1002/nsg.123001>
- Stoll J, Bigalke J, Grabner EW (1995) Electrochemical modelling of self-potential anomalies. *Surv Geophys* 16:107–120
- Sundararajan N, Srinivasa Rao P, Sunitha V (1998) An analytical method to interpret self-potential anomalies caused by 2D inclined sheets. *Geophysics* 63:1551–1555
- Sungkono, (2020) An efficient global optimization method for self-potential data inversion using micro-differential evolution. *J Earth Syst Sci* 129:178
- Vichabian Y, Morgan FD (2002) Self potentials in cave detection. *Lead Edge* 21:866–871
- Wynn JC, Sherwood SI (1984) The self-potential (SP) method: an inexpensive reconnaissance archaeological mapping tool. *J Field Archaeol* 11:195–204
- Xie J, Cui Y, Niu Q (2021) Coupled inversion of hydraulic and self-potential data from transient outflow experiments to estimate soil petrophysical properties. *Vadose Zone J* 20:e20157
- Yang XS (2010) A new metaheuristic bat-inspired algorithm. In: Nature inspired cooperative strategies for optimization (NICSO 2010). Springer, Berlin, Heidelberg, p 65–74
- Yang XS, He X (2013) Bat algorithm: literature review and applications. *Int J Bio-Inspir Com* 5:141–149
- Yüngül S (1950) Interpretation of spontaneous polarization anomalies caused by spherical ore bodies. *Geophysics* 15:237–246